

Structural Characterization of Phase Separation in Fe-Cr: A Current Comparison of Experimental Methods



XIN XU, JOAKIM ODQVIST, MAGNUS HÖRNQVIST COLLIANDER, MATTIAS THUVANDER, AXEL STEUWER, JOHAN E. WESTRAADT, STEPHEN KING, and PETER HEDSTRÖM

Self-assembly due to phase separation within a miscibility gap is important in numerous material systems and applications. A system of particular interest is the binary alloy system Fe-Cr, since it is both a suitable model material and the base system for the stainless steel alloy category, suffering from low-temperature embrittlement due to phase separation. Structural characterization of the minute nano-scale concentration fluctuations during early phase separation has for a long time been considered a major challenge within material characterization. However, recent developments present new opportunities in this field. Here, we present an overview of the current capabilities and limitations of different techniques. A set of Fe-Cr alloys were investigated using small-angle neutron scattering (SANS), atom probe tomography, and analytical transmission electron microscopy. The complementarity of the characterization techniques is clear, and combinatorial studies can provide complete quantitative structure information during phase separation in Fe-Cr alloys. Furthermore, we argue that SANS provides a unique *in-situ* access to the nanostructure, and that direct comparisons between SANS and phase-field modeling, solving the non-linear Cahn Hilliard equation with proper physical input, should be pursued.

DOI: 10.1007/s11661-016-3800-4

© The Author(s) 2016. This article is published with open access at Springerlink.com

I. INTRODUCTION

STAINLESS steels, which are based on the Fe-Cr binary alloy, are widely used in industrial applications because of their good mechanical properties and excellent corrosion resistance.^[1] However, ferrite- or martensite-containing stainless steels may undergo phase separation, *via* either nucleation and growth (NG) or spinodal decomposition (SD), and form Fe-rich (α) and Cr-rich domains (α') when they are thermally treated within the miscibility gap. Phase separation increases the hardness but decreases the impact toughness of the alloys, which could cause unexpected fracture in applications. Since alloys prone to this embrittlement are currently used in, for example, nuclear power generation and are being considered for new nuclear power

plants,^[2] brittle fracture must be avoided. The embrittlement phenomenon is known as “475 °C embrittlement” and, for instance, it limits the application temperature of duplex stainless steels to about 523 K (250 °C).^[3]

Due to the high technical relevance and its suitability as a model material for phase separation studies, binary Fe-Cr alloys have been extensively investigated. Theoretical tools such as phase-field modeling^[4–6] and kinetic Monte Carlo^[7–10] are frequently adopted to simulate the nanostructure evolution, and experimental tools such as Mössbauer spectroscopy (MS),^[11–14] transmission electron microscopy (TEM),^[4,5,15–17] small-angle neutron scattering (SANS),^[18–25] atom probe field ion microscopy (APFIM),^[7–9,26,27] and later atom probe tomography (APT)^[10,28–34] have been applied. Most of the studies in the literature focus on the rather late stages of phase decomposition, when the embrittlement is already severe, and today it is still considered a major challenge to quantitatively characterize the nanostructure in technically relevant cases, when the length-scale is in the order of a few atomic distances and the concentration variations between α and α' are only a few atomic percent.^[3,27,35]

The purpose of the present work is to compare and discuss currently available experimental methodologies for structural characterization of phase separation in Fe-Cr alloys. In prior work, some of the present authors have presented APT and TEM studies of phase

XIN XU, Ph.D. Student, and JOAKIM ODQVIST and PETER HEDSTRÖM, Associate Professors, are with the Department of Materials Science and Engineering, KTH Royal Institute of Technology, 100 44 Stockholm, Sweden. Contact e-mail: xinx@kth.se, pheds@kth.se. MAGNUS HÖRNQVIST COLLIANDER and MATTIAS THUVANDER, Associate Professors, are with the Department of Physics, Chalmers University of Technology, 412 96 Göteborg, Sweden. AXEL STEUWER, Professor, and JOHAN E. WESTRAADT, Senior Researcher, are with the Nelson Mandela Metropolitan University, Gardham Avenue, Port Elizabeth 6031, South Africa. STEPHEN KING, Principal Research Scientist, is with the ISIS Facility, Rutherford Appleton Laboratory, Didcot OX11 0QX, UK.

Manuscript submitted March 31, 2016.

Article published online October 14, 2016

separation in binary Fe-Cr alloys exposed to aging at 773 K (500 °C). The datasets from APT and TEM are discussed in relation to new SANS measurements, conducted on the same alloys under the same aging conditions. The relation to state-of-the-art structural modeling is also discussed.

II. EXPERIMENTAL METHODS FOR CHARACTERIZATION OF PHASE SEPARATION IN FE-CR ALLOYS

MS^[11–14] was one of the first experimental techniques applied to characterize the microstructural origin of the 748 K (475 °C) embrittlement phenomenon. MS probes the magnetic neighborhood of the ⁵⁷Fe isotope and it is very sensitive to small changes in the local environment. Most of the analyses in the literature consider the shift of the ferromagnetic peaks and thus the change of the hyperfine field. It is also possible to distinguish the evolution of the α' by studying the presence of a peak from the paramagnetic α' phase. The analysis of the paramagnetic peak can even be done for duplex steels, though it is difficult to separate the paramagnetic peaks of α' and austenite.^[13,14] It should be noted that the length-scale cannot be determined by MS. On the other hand, the high sensitivity of MS means that it can be used to investigate atomic short-range order, such as clustering above the miscibility gap.^[36]

The application of TEM,^[4,5,15–17] neutron diffraction (ND),^[37,38] and SANS^[23–25] to phase separation in Fe-Cr alloys is also well established. SANS can provide the length-scale of phase decomposition, whereas TEM and ND are used mainly as qualitative tools to detect whether phase separation has occurred. The application of APFIM to phase separation in Fe-Cr alloys has enabled the evaluation of both length-scale and concentration amplitude using the same method.^[26] More recently, there has been a tremendous development of APFIM towards the 3D atom probe (or APT).^[39] Today a standard APT dataset contains millions of atoms and the statistics are now sufficient to treat the early stages of phase decomposition by statistical means. The other structural characterization techniques have also undergone their own developments resulting in markedly improved performance or enhanced resolution, for example, the introduction of field-emission aberration corrected transmission electron microscopes, or the improved wavelength-resolution and broad simultaneous Q-range of spallation neutron source SANS instruments. These technical developments have also been utilized to investigate phase separation in Fe-Cr alloys.^[17,25]

Although there has been significant progress, each technique still has limitations. For instance, TEM is often considered to be the standard tool for investigating nano-scale microstructural features, but the analysis of the Fe-Cr system is particularly difficult. There is a very small difference in atomic size between Fe and Cr and their atomic scattering factors are similar; thus, the coherency is high and the phase contrast is very low.^[17]

It has been found that the decomposition can still be characterized by orienting the sample along its softest direction of the bcc crystal $\langle 100 \rangle$ where the minor coherency strains are best visualized.^[16] This approach is most effective in multicomponent alloys where the difference between α and α' phases may be slightly larger due to partitioning of the alloying elements.

APT is today considered to be the only technique capable of 3D atomic level chemical mapping, but the investigated volumes are small, typically in the order of $50 \times 50 \times 250 \text{ nm}^3$. The detection efficiency of a typical instrument today, the local electrode atom probe (LEAP), is below about 65 pct and thus almost half of the atoms are lost in the analysis.^[40] Interestingly, the very latest instruments have a detection efficiency of around 80 pct (for an instrument without energy compensation), promising some further improvement in the capability to observe the earliest stages of phase decomposition. Another factor to consider is that field evaporation in systems with more than one component involves complicated physics and it is difficult to perform 3D reconstructions and to ensure that the quantitative results are accurate on the nano-scale.^[40]

SANS has a more direct access to the average length-scale of the nano-scale phenomena in the bulk of polycrystals. However, the evaluation of concentration amplitude is not trivial and access to a suitable neutron facility is required. The latter is effectively rationed and can have a long lead time.

It is therefore rather evident that the application of a combination of the different experimental techniques is a far more robust way to generate a complete view of phase separation in Fe-Cr. In the following text, we present new SANS measurements and analysis, conducted using a pulsed neutron source and the time-of-flight technique, which allows the detection of phase separation over a wide range of length scales simultaneously, and compare these results with our prior measurements using TEM and APT.^[17,29,32]

III. EXPERIMENTAL DETAILS

A. Materials

All the experiments presented in the present work (TEM, APT, and SANS) were conducted on the same three binary Fe-Cr alloys with different Cr contents, see Table I. The alloys were prepared by vacuum arc melting and solution treatment at 1373 K (1100 °C) for 2 hours in a slight overpressure of pure argon before being quenched in brine. Thereafter, samples were aged at 773 K (500 °C) for different times and quenched in brine.

B. SANS Measurements

Samples for SANS measurements were cut into plates with the approximate dimensions $5 \times 5 \times 1.5 \text{ mm}^3$, and the oxide layer was removed by grinding and polishing. SANS data were then recorded on the LOQ diffractometer at the ISIS pulsed neutron source, Oxfordshire,

Table I. Chemical Composition of the Binary Fe-Cr Alloys (Weight Percent) and the Isothermal Aging Times at 773 K (500 °C)

Alloy	Code	Cr	C	Si	Mn	S	P	N	Ni	Fe	Aging Time (h)
Fe-25Cr	25Cr100	25.28	0.002	0.09	0.005	0.006	0.004	0.009	0.03	bal.	100
	25Cr1000										1000
Fe-30Cr	30Cr20	30.42	0.004	0.11	0.008	0.008	0.006	0.006	0.02	bal.	20
	30Cr200										200
Fe-35Cr	35Cr1	36.10	0.005	0.09	0.006	0.005	0.005	0.008	0.02	bal.	1
	35Cr10										10
	35Cr100										100

UK. The wavelength, λ , range of the incident neutron beam was 2.2 to 10 Å, allowing a range of the scattering vector (Q) from 0.006 to 1.4 Å⁻¹ ($Q = 4\pi\sin\theta/\lambda$, where 2θ is the scattering angle) to be measured simultaneously. Samples were fixed at around 11 m from the moderator. Two detector banks were used to collect data. An ORDELA multi-wire proportional gas counter located at 4.15 m from the sample, and an annular scintillator area detector located at 0.6 m from the sample. The active area of the former detector was 64 × 64 cm² with 5 mm square pixels, whilst the latter had 12 mm pixels.^[41] All the measurements were performed at ambient temperature using a neutron beam collimated to 4 mm diameter. Scattering data of as-quenched samples were collected for 2 hours per sample and that from the aged samples were collected for 30 minutes per sample.

The raw SANS data were corrected for the measured neutron transmission of the samples, illuminated volume, instrumental background scattering, and the efficiency and spatial linearity of the detectors to yield the macroscopic coherent differential scattering cross section ($d\Sigma/d\Omega$) using the MantidPlot framework (version 3.2.1). These reduced instrument-independent data were then placed on an absolute scale using the scattering from a standard sample (a partially deuterated polymer blend of known molecular weight) measured with the same instrument settings.^[42] $d\Sigma/d\Omega$ describes the shapes and sizes of the scattering bodies in the sample and the interactions between them.^[41]

C. APT Measurements

The final preparation of samples for APT measurements was performed by the standard two-step electro-polishing method. APT analyses were conducted using a LEAP 3000X HRTM at 55 K (−218 °C). The ion detection efficiency is about 37 pct. The 3D reconstructions were performed by IVAS 3.4.3 software with evaporation field of 33 V/nm, field factor (k_f) 3.8 and image compression factor 1.8. Most of the analyses have been presented earlier and further details can be found in the following references.^[29,32,43] To complement these data, new measurements were conducted for sample 35Cr1.

D. TEM Measurements

The first part of the TEM study was conducted using phase contrast in a JEOL 2000F TEM^[16] operating at 200 kV. The samples were prepared by electro-polishing

and subsequently immediately transferred to the high vacuum system to avoid any oxide formation that could obstruct the visualization of the phase contrast arising due to coherency strains. The second part of the TEM study was performed using a double Cs corrected JEOL ARM 200F TEM operating at 200 kV.^[17] The samples were prepared in two different ways: (i) electro-polishing and subsequent gentle Ar ion beam polishing, (ii) lift-out technique in a Helios NanoLab focused ion beam scanning electron microscope (FIB-SEM). The TEM analyses, conducted using the JEOL ARM 200F microscope, were performed by mainly electron energy loss spectroscopy (EELS) spectrum imaging (SI).

The chromium and iron elemental maps were extracted by performing windowed elemental mapping on the 3D data cube. Multi-linear least squares (MLLS) fitting was performed using the extracted background of the high-loss region and reference spectra for the chromium and iron signals over the energy range from 400 to 900 eV. The periodic length-scale was investigated using auto-correlation analysis on the compositional maps in Digital MicrographTM.

IV. RESULTS

A. SANS Results

SANS data for the different alloys and aging conditions are shown in Figure 1. It can be seen that peaks appear in the SANS patterns of all the aged samples. This arises from correlations in density within the alloy nanostructure and is a characteristic of phase separation. The patterns of solution treated (as-quenched) samples have no clear peak. They are flat in the Q range larger than 0.1 Å⁻¹ and they almost overlap with each other (Figure 1(d)).

In order to assess the peak position Q_m and peak intensity $d\Sigma(Q_m)/d\Omega$, the scattering from the decomposed structure was evaluated according to the method illustrated in Figure 2. Since the patterns of the as-quenched samples, *i.e.*, structures without decomposition, show a flat behavior beyond $Q = 0.1$ Å⁻¹ and no interaction peak, their scattering function was taken as the scattering pattern of a homogeneous sample. $d\Sigma(Q)/d\Omega$ of the as-quenched sample was fitted by a power function (I_b), as shown in Figure 2(a), and subsequently the background of each condition was subtracted, see Figure 2(b). $d\Sigma(Q)/d\Omega$ was normalized by I_b , $I_n = d\Sigma(Q)/d\Omega/I_b$ (Figure 2(c)) and I_n vs $\log Q$ was fitted by

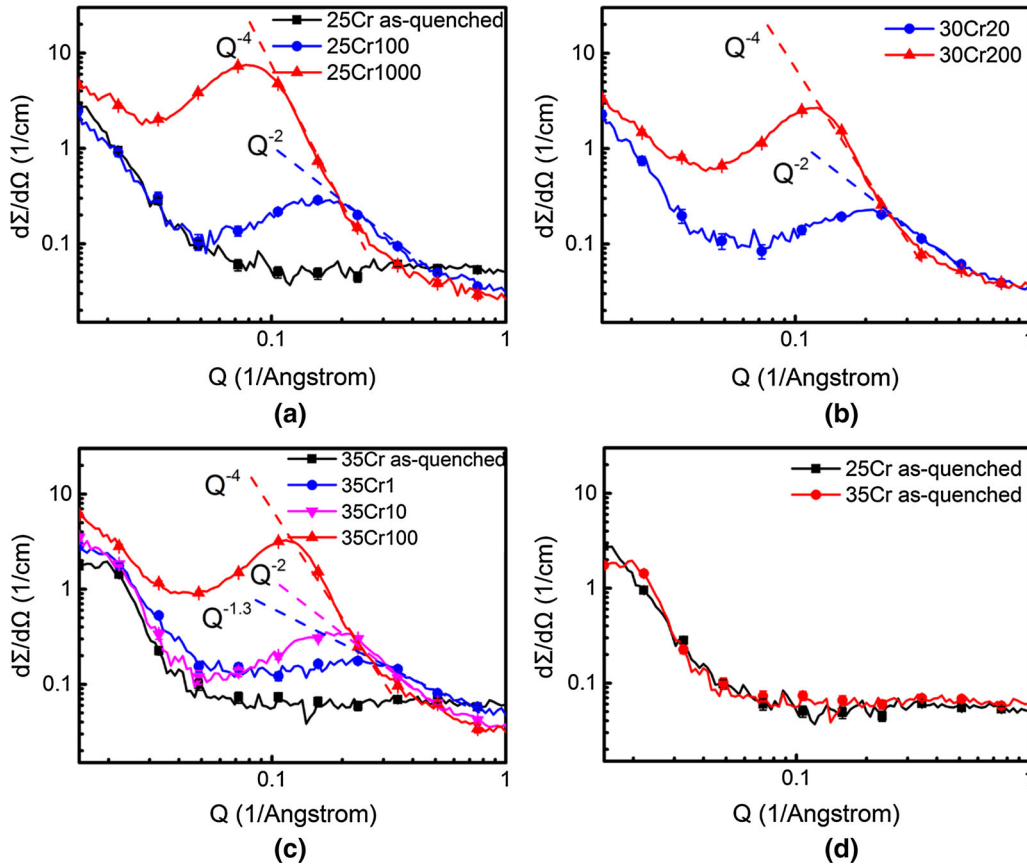


Fig. 1—SANS patterns of (a) 25Cr, (b) 30Cr, and (c) 35Cr alloys after different heat treatments, and (d) the comparison of the scattering patterns from as-quenched samples (some error bars are covered by symbols) (Color figure online).

a Gaussian function, I_G . Finally, the intensity characteristic of phase separation, I_{PS} , was obtained by $I_{PS} = I_b(I_G - 1)$, see Figure 2(d). Q_m and $d\Sigma(Q_m)/d\Omega$ were determined from the pattern of I_{PS} . The procedure explained here is similar to the procedure used in Hörnqvist *et al.*^[25] with the exception of the fit of the background which was performed for each condition in the present study since the scattering behavior of the initial states was different.

As can be seen from Figure 3, $d\Sigma(Q_m)/d\Omega$ increases with aging time (Figure 3(a)) and Q_m moves to smaller reciprocal length-scale (Q), *i.e.*, longer real-space length scales (Figure 3(b)), as phase separation progresses. This is also seen from Figure 1. Since the initial stages of phase separation are particularly difficult to address experimentally, it is interesting to turn the attention to what happens with the scattering function beyond the peak position. The value of $d\Sigma(Q)/d\Omega$ decreases in the high- Q range for all the aged samples, but, as mentioned, the scattering patterns of the unaged samples are flat (Figure 1). The Q -dependence of the scattering functions for samples 25Cr1000, 30Cr200, and 35Cr100 in the high- Q range is similar to each other, at about -4 . The Q -dependence of the scattering patterns for samples 25Cr100, 30Cr20, and 35Cr10 is, on the other hand, close to -2 , while the Q -dependence of sample 35Cr1 is about -1.3 . Thus, it is clear that the slope of the scattering function in the high- Q range is a rather

sensitive probe of the early-stage phase separation. The slope increases gradually from zero for the solution-treated sample to -4 for all the samples that are significantly decomposed, *i.e.*, after long time aging at 773 K (500 °C). This Q -dependence is related to the degree of segregation in the emerging interface (through *e.g.*, the surface fractal dimension), a more negative slope representing greater segregation.

If it is assumed that all alloys decompose *via* SD, the wavelength of decomposition can be calculated by the formula generated by substituting $Q = 4\pi\sin\theta/\lambda$ into Bragg's Law:

$$d = \frac{2\pi}{Q_m}, \quad [1]$$

where Q_m is the scattering vector at the peak position. The calculated wavelengths are shown in Table II together with the wavelengths calculated from APT using the radial distribution function (RDF) and the auto-correlation function (ACF),^[32] and from TEM using the ACF.^[16,17] The amplitude for the 35Cr alloy from APT and TEM is also shown.

It should be noted that it has previously been found by APT that the three investigated alloys are in the transition region between NG and SD at 773 K (500 °C)^[29] and although Pareige *et al.*^[10] claimed that Fe-25 at. pct Cr decomposed *via* SD, isolated particles

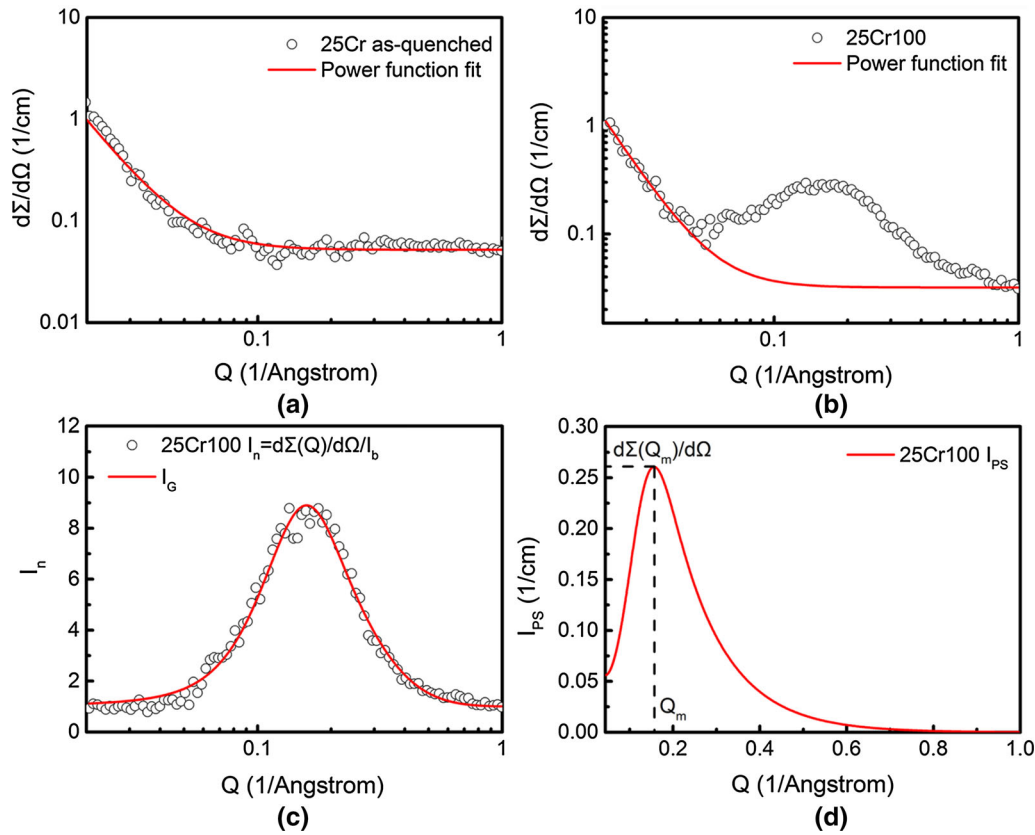


Fig. 2—Example of the analysis method to evaluate peak position Q_m and peak intensity $d\Sigma(Q_m)/d\Omega$ (Color figure online).

have been shown on 3D atom maps in both References 10 and 29. It is therefore believed that the dominant decomposition mechanism in alloy 25Cr is non-classical NG.^[29] Henceforth, it may be better to treat this condition using a precipitate analysis. The Guinier approximation ($\ln(d\Sigma(Q)/d\Omega)$ vs Q^2) is commonly used to estimate the size of particles in alloys, and relies on the fact that at low Q values the scattering law for a sphere may be approximated by an exponential series expansion.^[44] The radius of gyration or the Guinier radius, R_g , can be calculated from the slope of the plot, which is equal to $-R_g^2/3$. If we assume that the microstructure consists of monodisperse spherical particles, the radius of the particles, R , is equal to $\sqrt{5/3}R_g$.^[44] The same particle approximation was also applied to the other alloys in this work for comparison. The appearance of the Guinier plots for the different alloys was similar and the behavior is exemplified for alloy 25Cr in Figure 4. The particle radii calculated from the Guinier plots are presented in Table III. The calculated particle size shows the same trend as the spinodal wavelengths presented in Table II, namely, that the apparent domain size increases as phase separation progresses.

It is interesting to evaluate the evolution of the structural parameters with time in comparison with theoretical works. The theory of Binder *et al.*^[45] and the Monte Carlo simulations of Marro *et al.*^[46,47] have demonstrated that the time evolution of the peak position and the peak intensity obey power laws:

$$Q_m \propto t^{-a'} \quad [2]$$

$$\frac{d\Sigma}{d\Omega}(Q_m) \propto t^{a''}, \quad [3]$$

where t is the aging time.

The a' and a'' parameters were evaluated for the 35Cr alloy since this is the only alloy where a sufficient number of sample conditions were investigated to provide a fair description of the kinetic coefficients. The values of a' and a'' are 0.16 and 0.64, respectively. Since the wavelength is proportional to Q_m^{-1} , the wavelength is proportional to $t^{a'}$, and thus, the wavelength of alloy 35Cr at 773 K (500 °C) has a $t^{0.16}$ dependence. The values of a' and a'' in the present work are in good agreement with the work by Katano *et al.*^[19] Ujihara *et al.*^[24] measured $a' = 0 - 0.35$ and they also observed that a' was smaller at lower aging temperature for the same alloy. Moreover, they found that Q_m did not always have a power law dependence with t , and a' was smaller in the early stages of decomposition. Theoretically, Binder *et al.*^[45] predicted $a' = 1/6$ and $a'' = 1/2$ for low temperatures, while Marro *et al.*^[46,47] obtained $a' = 0.2 - 0.28$ and $a'' = 0.65 - 0.74$ below the critical temperature T_c . The value of a' obtained in the present work is slightly smaller than the theoretical estimations. The reason may be that the decomposition is still in the early stage. If, instead, the kinetics is evaluated based on the particle size showed in Table III,

the particle size evolves with a simple power law according to $R \propto t^{0.27}$. The theory of Lifshitz–Slyozov–Wagner^[48,49] indicates $a' = 1/3$ in the coarsening stage occurring after long-term aging when the

diffusion is mainly through the bulk. Huse^[50] argued that smaller a' observed at short aging times was due to the contribution of the diffusion along the interface. Some later simulation works showed agreements with their theories.^[10,51,52] The above results illustrate that in order to reveal the mechanism of decomposition, it may be necessary to make careful comparisons of the kinetic evolution of the microstructure characteristic length-scale with physical models.

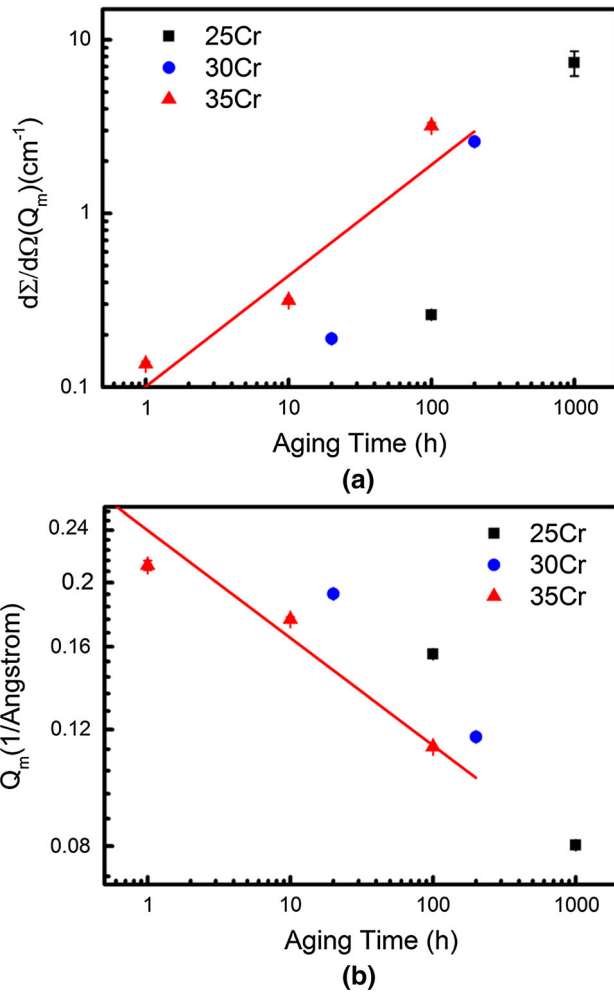


Fig. 3—Evolution of (a) peak intensity $d\Sigma(Q_m)/d\Omega$ and (b) peak position Q_m of SANS patterns with aging time. Only the data of 35Cr alloy were fitted by a power law function (Color figure online).

B. Summary of TEM and APT Results

TEM elemental mapping (EELS) results for alloy 35Cr in unaged and aged conditions are presented in Figure 5. There is already a slight indication of elemental segregation after 1 hours of aging at 773 K (500 °C) and after 10 hours aging and onwards phase separation is evident. These results presented comprehensively in Reference 17 were surprising, since it was generally believed that the many overlapping domains that the electron beam was traveling through would cause an averaging of the elemental, Cr and Fe, signal and that the nanostructure could not be visualized. It should be mentioned that the elemental mapping in Figure 5 was conducted on rather thick samples (thickness ≈ 42 –100 nm) and still it was possible to resolve the decomposed regions of about 2 nm in sample 35Cr1. The reason was hypothesized to be that the main part of the signal arises in the top surface (<5 nm) of the sample before the electron beam has spread out significantly, reducing the signal notably.^[17] The estimation of the wavelength of decomposition was found to be insensitive to the thickness of the TEM sample, whereas the amplitude of decomposition was only possible to estimate using a much thinner sample of about 32 nm thickness and for the sample aged for 100 hours.^[17]

2D Cr concentration maps sectioned from the APT measurements on the 35Cr alloy are presented in Figure 6. It can be seen that there is greater segregation, *i.e.*, into α and α' , after 10 and 100 hours of aging at 773 K (500 °C), compared to the unaged sample and the sample aged for 1 hour. By applying statistical analysis, it is possible to distinguish a difference also between the unaged sample and the sample that has been aged for

Table II. Spinodal Wavelengths and Amplitude Obtained by Different Methods

Methods	Fe-25Cr		Fe-30Cr		Fe-35Cr		
	25Cr100	25Cr1000	30Cr20	30Cr200	35Cr1	35Cr10	35Cr100
Spinodal Wavelength (nm)							
SANS	4.0 ± 0.03	7.8 ± 0.02	3.3 ± 0.04	5.4 ± 0.02	3.0 ± 0.05	3.6 ± 0.03	5.6 ± 0.02
APT, RDF	5.4	7.8	4.2	6	4.1	3.8	5.2
APT, ACF	3.0	6.5	3.5	4.75		3.5	4.5
TEM		5 to 10*			2**	3**	6**
Amplitude (At Pct)							
APT, RDF	17.5	54.0	16.6	43.8	13.6***	20.1	35.4
APT, LBM	9.5	23.4	9.3	19.2		10.7	17.7
TEM							25**

APT data are from Ref. [32], LBM: Langer-Bar-on-Miller theory. * Ref. [16]; ** Ref. [17]; ***Calculated by Eq. [7] in Ref. [32]

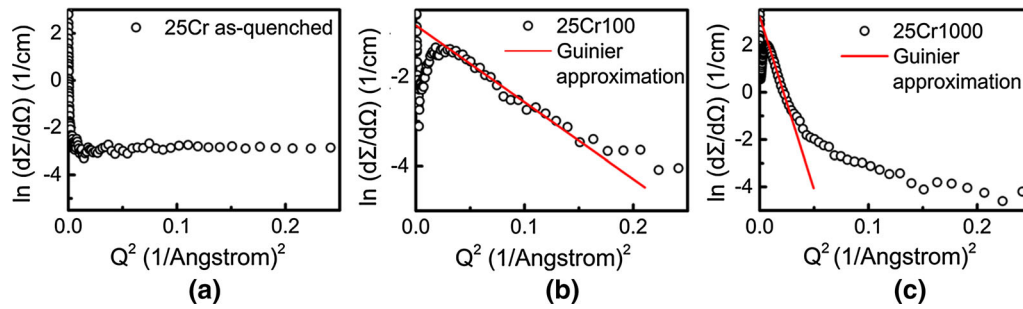


Fig. 4—Guinier plots of 25Cr alloy: (a) as-quenched, (b) 25Cr100, (c) 25Cr1000 (Color figure online).

Table III. Guinier and Particle Size Values Calculated from Guinier Plots

	Fe-25Cr		Fe-30Cr		Fe-35Cr		
	25Cr100	25Cr1000	30Cr20	30Cr200	35Cr1	35Cr10	35Cr100
R_g (nm)	0.72	2.10	0.60	1.55	0.46	0.74	1.58
R (nm)	0.93	2.71	0.78	2.00	0.59	0.96	2.04

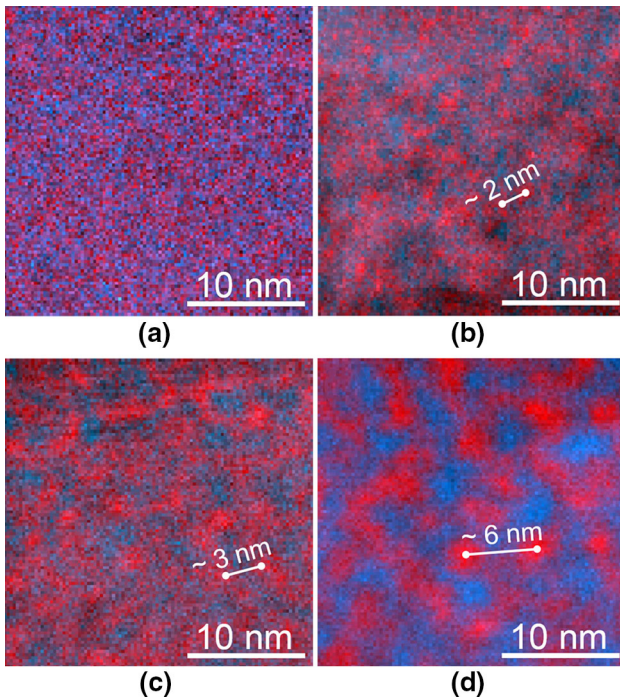


Fig. 5—Analytical TEM composite elemental maps (EELS) of multi-linear least squares (MLLS) fitting coefficients for the Cr-signal (red) and Fe-signal (blue) for alloy 35Cr aged at 773 K (500 °C) for different times^[17]: (a) 0 h, (b) 1 h, (c) 10 h, and (d) 100 h. The estimated wavelength is schematically marked on the figures (Color figure online).

1 hour at 773 K (500 °C). It has been found that one of the most sensitive ways to represent minor decomposition is by generating the radial concentration profiles from each and every Cr atom in the analyzed volume and then averaging these concentration profiles. This treatment is called RDF analysis and example results are given in Figure 7 for the 35Cr alloy aged at 773 K

(500 °C). It is clear that all alloy conditions are distinct from each other and the wavelength and amplitude of the concentration fluctuations can be evaluated from these curves using the method suggested by Zhou *et al.*^[32] The results from the RDF analysis of wavelength and amplitude are included in Table II. It should be noted that when the nominal alloy composition is not in the center of the miscibility gap, as in the case of the alloys in the present work, an asymmetric compositional amplitude develops.

V. DISCUSSION

A. SANS Function Evolution During Aging

The decomposition after 1 hour aging of alloy 35Cr is clearly seen from the SANS measurements (Figure 1), demonstrating the sensitivity of SANS to small degrees of decomposition. Studies of the early stages of decomposition require good resolution at the high- Q range, since the change in slopes of $d\Sigma/d\Omega$ is a good indicator of decomposition. A similar type of scattering behavior has been found previously by Furusaka *et al.*^[20] They studied phase separation in Fe-Cr alloys and Al-6.8pctZn at different aging conditions (aging times up to 50 hours for Fe-40pctCr and up to 60 minutes for Al-6.8pctZn at different temperatures). They observed only Q^{-2} and Q^{-4} dependences of the scattering function at high- Q ranges. It was believed that early and late stages of phase separation can be distinguished clearly by these two features. They argued that the Q^{-2} dependence is a feature of the early stages of phase separation, and the Q^{-4} dependence characterizes the later stages of phase separation when the inhomogeneities in the alloys have sharp interfaces with the matrix. Ujihara *et al.*^[24] also observed the same Q^{-n} dependence. However, a recent *in-situ* SANS work shows a gradual increase of the slope with aging time

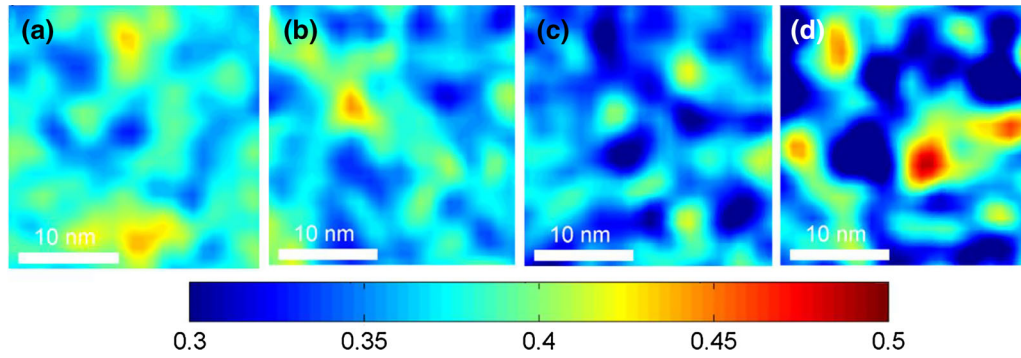


Fig. 6—APT 2D Cr-concentration maps of alloy 35Cr alloy aged at 773 K (500 °C): (a) unaged, (b) 1 h, (c) 10 h, and (d) 100 h, part of the results from Ref. [29] (Color figure online).

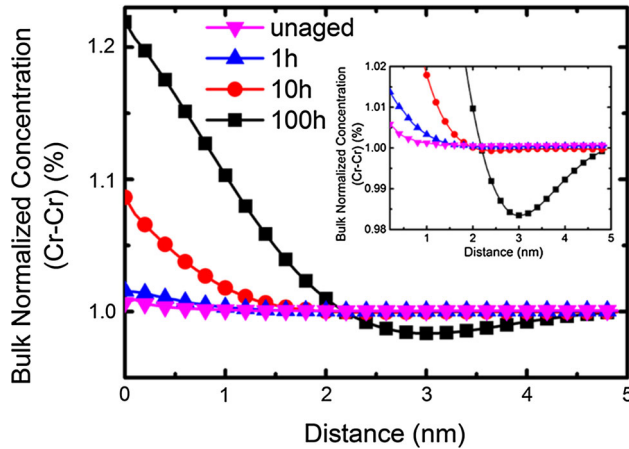


Fig. 7—Radial distribution functions from APT data for the 35Cr alloy aged at 773 K (500 °C), part of the results from Ref. [29]. The inset shows a magnification in order to make the difference between the unaged sample and the sample aged for 1 h clearer (Color figure online).

from 0 to 2 at 773 K (500 °C) and from 0 to 2.5 at 798 K (525 °C) for alloy 35Cr.^[25] The results presented here agree well with this *in-situ* work. It should be pointed out that a sharp interface, defined here as either NG or coarsening of SD, is not a pre-requisite for the Q^{-4} dependence since it is known from APT^[29,32] that all conditions in the present work are far from the late stage with a fully developed amplitude and the interfaces between Fe-rich and Cr-rich domains are still diffuse. Therefore, one must not draw too far-reaching conclusions on interfaces based on the slopes since they can be affected by several factors.^[24]

It is interesting to note that no distinct difference in scattering function evolution could be found for the different alloys. It is believed that the three investigated alloys are located in the transition region between NG and SD, but alloy 25Cr, which is decomposing *via* non-classical NG, displays a similar scattering function evolution as the two other alloys, *i.e.*, 30Cr and 35Cr, which are decomposing *via* SD.^[29] Similar scattering functions for particle and spinodal microstructures have also been found before.^[24,53,54] Furthermore, it seems like the analysis of structural parameters, using either the particle or composition wave assumption, is

reasonable for all alloy conditions. This may indicate that these alloys have features of both NG and SD. On the other hand, it may also indicate that SANS is not able to distinguish between different mechanisms of decomposition, unless kinetics is considered.

B. Comparison Between SANS, TEM, and APT

It is generally believed that TEM is not a suitable technique^[27] to investigate the early stages of phase separation in Fe-Cr since the concentration fluctuations are minute, both in length-scale and in concentration amplitude. TEM has instead mainly been used as a qualitative probe^[5] though in some cases the mechanism of decomposition has been distinguished, for example, where the phase contrast is larger, enabling the observation of particles or mottled contrast characteristic for SD.^[55] Comparing the results herein from TEM and APT with the SANS, it is clear that all techniques are capable of detecting the early stages of phase separation in the Fe-Cr system.

Table II and Figure 8 show the comparison between the wavelengths obtained from SANS, TEM, and APT data. It can be seen that the spinodal wavelength calculated from the SANS measurements is consistent with both prior TEM and APT results. The wavelengths obtained from the RDF analysis of APT data are, however, generally larger than the values from SANS while wavelengths obtained from the ACF are generally smaller than that from SANS. Zhou *et al.*^[32] suggested that the RDF is a good tool for estimating the wavelength and amplitude of phase separation. However, for the very early stages of, for example, 35Cr1, the wavelength obtained by RDF seems incorrect. It is larger than that from SANS and even slightly larger than the wavelength of 35Cr10 from the RDF. As mentioned earlier, the APT measurements are only performed on a very small volume and there are some uncertainties regarding the 3D reconstruction, and thus the good agreement with SANS validates the use of the APT technique for determining the wavelength even though SANS is deemed to be more reliable. The ACF analysis of the APT data was only performed in 1D but still the agreement is good, and thus the assumed isotropic nature of the microstructure seems reasonable.

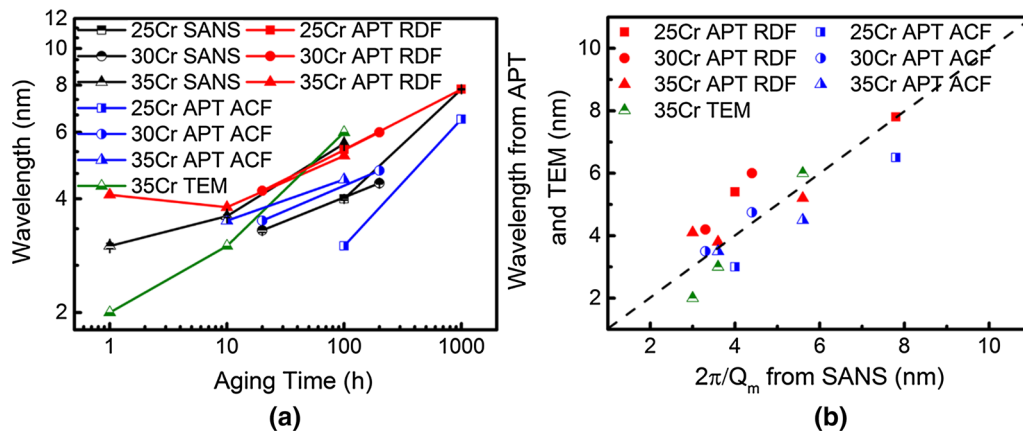


Fig. 8—Wavelengths of SD in Fe-Cr system calculated from SANS data compared with APT and TEM results (Color figure online).

On the other hand, it should be noted that the thickness of the thin-foils used for analytical TEM is in the order of 100 nm, which is much larger than the wavelength measured.^[17] Moreover, the wavelength quantified by TEM remains constant for different thicknesses. Therefore, as Westraadt *et al.*^[17] have indicated, the EELS signal is not averaged through the thickness of the samples.

For quantifying the amplitude of phase separation, APT is a good choice. Different methods have been proposed for estimating the amplitude from APT data. RDF was suggested as a promising method to give accurate results on the composition amplitude in Fe-Cr alloys.^[32] Westraadt *et al.*^[17] used the standard deviation in the relative quantification maps from TEM to represent the amplitude of a 35Cr alloy as shown in Table II. Nevertheless, the composition fluctuation amplitude measured from the EELS analysis varies with the foil thicknesses and the acquisition parameters. Only approximate numbers were given from the EELS analyses, since the electron-sample interaction volume generates some uncertainty between the elemental distribution in the sample and the compositional measurement. The required thickness for obtaining a reasonable amplitude is related to the mean free path for inelastic scattering of electrons.^[17,56] The reasonable agreement is achieved only when the thickness was reduced to 32 nm for 35Cr100. Further reduction in the sample thickness reduces the probability of a scattering event, resulting in a low signal-to-noise elemental map. To determine the amplitude for samples with less decomposition is even harder since preparing thinner samples is a challenge. In the present work, the amplitude was not calculated from the SANS data because of the lack of an effective method for doing so.

Despite the shortcomings in determining composition amplitudes, both TEM and SANS are competitive tools for characterizing phase separation. TEM provides microstructure images which reflect the microstructure directly and are helpful in interpreting APT and SANS results. With TEM crystal orientations are available, which is hard to acquire from APT. Crystal orientations are of significant importance when investigating

anisotropic decomposition, *e.g.*, decomposition under coherency strains.^[57–61] When there are coherency strains, phase separation prefers to develop along specific crystal directions, the soft directions.^[59] This leads to anisotropic decomposition in materials. Soriano-Vargas *et al.*^[5] observed that α' aligned in the $\langle 110 \rangle$ direction of α by TEM. Although anisotropic decomposition in single crystalline or textured polycrystalline materials can be analyzed by SANS, orientations of the single crystal or the texture of the polycrystal should be determined before measurements and measurements should be done along known orientations to quantify the analyses.^[60,61] Otherwise, TEM is still needed after SANS measurements to confirm the reason for the anisotropy. This also applies to APT when using it to study anisotropic decomposition. Therefore, combination of TEM, APT, and SANS can give an unambiguous view on anisotropic phase separation. Moreover, combining microstructure images from TEM and APT (especially the 3D atom map) may give more impartial views when drawing conclusions on the decomposed microstructure from SANS data since from SANS it is hard to distinguish between different morphologies during phase separation as discussed above. On the other hand, SANS can collect data efficiently and has great advantages over the other two techniques for *in-situ* analyses, which enable us to continuously track the development of phase separation.^[22,25,62] These advantages of SANS can be utilized for effective kinetic analysis to provide a more comprehensive understanding of the kinetics of phase separation at an early stage of embrittlement.

One of the major benefits of SANS is arguably the direct mapping of the reciprocal space structure, which can also be obtained from modeling *e.g.*, by LBM.^[63–65] A recent example of investigations on the kinetics of the early stage of phase separation can be found in Hörnqvist *et al.*^[25] They used *in-situ* SANS measurements to study the evolution of the microstructure at 773 K (500 °C) and 798 K (525 °C) and compared the results with modeling using the Cahn–Hilliard–Cook (CHC) model. They found a good agreement of the length scale of decomposition between experiments and

modeling. The linearized CHC theory is not sufficient to accurately describe the phase transformation. Nonetheless, the examples from Bley^[23] and Hörnqvist *et al.*^[25] demonstrate the link between the Cahn-Hilliard model and SANS experiments. Hence, by simulating the structure factor evolution using the non-linear Cahn-Hilliard model with proper physical input data, and making direct comparisons to the structure factors from SANS where the nuclear scattering has been deconvoluted,^[23] it could be possible to significantly advance our understanding, and the quantitative modeling, of the phase separation process. The recent development in phase-field modeling of SD^[43,66] enables physical descriptions of binary as well as multicomponent alloy systems considering all the physical parameters and thermodynamics appropriately.

VI. SUMMARY

In the present paper, we have discussed different experimental techniques for the characterization of structure evolution during phase separation in Fe-Cr alloys. Small-angle neutron scattering (SANS), atom probe tomography (APT), and transmission electron microscopy (TEM) were treated in some detail. All three techniques are valuable in the quest for understanding phase separation, and the factors influencing phase separation, in Fe-Cr alloys. There are clearly limitations with all techniques and the most comprehensive, reliable view of the microstructure evolution, *i.e.*, evolution of characteristic length-scale, composition amplitude, and crystallographic as well as morphological aspects, can be obtained by a combination of the three. Furthermore, we argue that SANS provides a unique capability since it is the only technique able to study the kinetics of phase separation in the Fe-Cr system *in-situ* during thermal treatments. It is also possible to investigate the early stages of phase decomposition, which is of primary technical interest. SANS also has a link to state-of-the-art materials modeling and direct comparisons between SANS and phase-field modeling, solving the non-linear Cahn-Hilliard equation using accurate thermodynamic descriptions, should be pursued.

ACKNOWLEDGMENTS

This work was performed within the VINN Excellence Center Hero-m, financed by VINNOVA, the Swedish Governmental Agency for Innovation Systems, Swedish industry and KTH Royal Institute of Technology. X. Xu acknowledges the support from the China Scholarship Council (CSC). The access to the LOQ beamline at ISIS for SANS measurements was provided through Proposal No. RB 1320394 courtesy of the United Kingdom Science & Technology Facilities Council. The transmission electron microscopy investigations in the present work were conducted at the Centre for High Resolution TEM at Nelson Mandela Metropolitan University, South Africa.

OPEN ACCESS

This article is distributed under the terms of the Creative Commons Attribution 4.0 International License (<http://creativecommons.org/licenses/by/4.0/>), which permits unrestricted use, distribution, and reproduction in any medium, provided you give appropriate credit to the original author(s) and the source, provide a link to the Creative Commons license, and indicate if changes were made.

REFERENCES

1. K.H. Lo, C.H. Shek, and J.K.L. Lai: *Mater. Sci. Eng. R Rep.*, 2009, vol. 65, pp. 39–104.
2. I. Cook: *Nat. Mater.*, 2006, vol. 5, pp. 77–80.
3. N. Pettersson, S. Wessman, M. Thuvander, P. Hedström, J. Odqvist, R.F.A. Pettersson, and S. Hertzman: *Mater. Sci. Eng. A*, 2015, vol. 647, pp. 241–48.
4. O. Soriano-Vargas, E.O. Avila-Davila, V.M. Lopez-Hirata, H.J. Dorantes-Rosales, and J.L. Gonzalez-Velazquez: *Mater. Trans.*, 2009, vol. 50, pp. 1753–57.
5. O. Soriano-Vargas, E.O. Avila-Davila, V.M. Lopez-Hirata, N. Cayetano-Castro, and J.L. Gonzalez-Velazquez: *Mater. Sci. Eng. A*, 2010, vol. 527, pp. 2910–14.
6. W. Xiong, K.A. Grönhagen, J. Ågren, M. Selleby, J. Odqvist, and Q. Chen: *Solid State Phenom.*, 2011, vols. 172–174, pp. 1060–65.
7. M.K. Miller, J.M. Hyde, M.G. Hetherington, A. Cerezo, G.D.W. Smith, and C.M. Elliott: *Acta Metall. Mater.*, 1995, vol. 43, pp. 3385–3401.
8. J.M. Hyde, M.K. Miller, M.G. Hetherington, A. Cerezo, G.D.W. Smith, and C.M. Elliott: *Acta Metall. Mater.*, 1995, vol. 43, pp. 3403–13.
9. J.M. Hyde, M.K. Miller, M.G. Hetherington, A. Cerezo, G.D.W. Smith, and C.M. Elliott: *Acta Metall. Mater.*, 1995, vol. 43, pp. 3415–26.
10. C. Pareige, M. Roussel, S. Novy, V. Kuksenko, P. Olsson, C. Domain, and P. Pareige: *Acta Mater.*, 2011, vol. 59, pp. 2404–11.
11. H. Yamamoto: *Jpn. J. Appl. Phys.*, 1964, vol. 3, pp. 745–48.
12. H. Kuwano, Y. Ishikawa, T. Yoshimura, and Y. Hamaguchi: *Hyperfine Interact.*, 1992, vol. 69, pp. 501–04.
13. C. Lemoine, A. Fnidiki, J. Teillet, M. Hédin, and F. Danoix: *Scr. Mater.*, 1998, vol. 39, pp. 61–66.
14. C. Lemoine, A. Fnidiki, F. Danoix, M. Hédin, and J. Teillet: *J. Phys. Condens. Matter*, 1999, vol. 11, pp. 1105–14.
15. R. Lagneborg: *ASM Trans. Quart.*, 1967, vol. 60, pp. 67–78.
16. P. Hedström, S. Baghsheikhi, P. Liu, and J. Odqvist: *Mater. Sci. Eng. A*, 2012, vol. 534, pp. 552–56.
17. J.E. Westraadt, E.J. Olivier, J.H. Neethling, P. Hedström, J. Odqvist, X. Xu, and A. Steuwer: *Mater. Charact.*, 2015, vol. 109, pp. 216–21.
18. Y.Z. Vintaykin, V.B. Dmitriyev, and V.Y.U. Kolontsov: *Fiz. Met. Met.*, 1969, vol. 27, pp. 1131–33.
19. S. Katano and M. Izumi: *Phys. B + C*, 1983, vol. 120, pp. 392–96.
20. M. Furusaka, Y. Ishikawa, and M. Mera: *Phys. Rev. Lett.*, 1985, vol. 54, pp. 2611–14.
21. J.C. LaSalle and L.H. Schwartz: *Acta Metall.*, 1986, vol. 34, pp. 989–1000.
22. K.A. Hawick, J.E. Epperson, C.G. Windsor, and V.S. Rainey: *MRS Proc.*, 1990, vol. 205, p. 107.
23. F. Bley: *Acta Metall. Mater.*, 1992, vol. 40, pp. 1505–17.
24. T. Ujihara and K. Osamura: *Acta Mater.*, 2000, vol. 48, pp. 1629–37.
25. M. Hörnqvist, M. Thuvander, A. Steuwer, S. King, J. Odqvist, and P. Hedström: *Appl. Phys. Lett.*, 2015, vol. 106, pp. 061911-1-5.
26. S.S. Brenner, M.K. Miller, and W.A. Soffa: *Scr. Metall.*, 1982, vol. 16, pp. 831–36.
27. F. Danoix and P. Auger: *Mater. Charact.*, 2000, vol. 44, pp. 177–201.

28. S. Novy, P. Pareige, and C. Pareige: *J. Nucl. Mater.*, 2009, vol. 384, pp. 96–102.
29. W. Xiong, P. Hedström, M. Selleby, J. Odqvist, M. Thuvander, and Q. Chen: *Calphad Comput. Coupling Phase Diagr Thermochem.*, 2011, vol. 35, pp. 355–66.
30. J. Zhou, J. Odqvist, M. Thuvander, S. Hertzman, and P. Hedström: *Acta Mater.*, 2012, vol. 60, pp. 5818–27.
31. P. Hedström, F. Huyan, J. Zhou, S. Wessman, M. Thuvander, and J. Odqvist: *Mater. Sci. Eng. A*, 2013, vol. 574, pp. 123–29.
32. J. Zhou, J. Odqvist, M. Thuvander, and P. Hedström: *Microsc. Microanal.*, 2013, vol. 19, pp. 665–75.
33. J. Zhou, J. Odqvist, L. Höglund, M. Thuvander, T. Barkar, and P. Hedström: *Scr. Mater.*, 2014, vol. 75, pp. 62–65.
34. P. Maugis, Y. Colignon, D. Mangelinck, and K. Hoummada: *JOM*, 2015, vol. 67, pp. 2202–07.
35. F. Findik: *Mater. Des.*, 2012, vol. 42, pp. 131–46.
36. S.M. Dubiel and J. Cieslak: *Phys. Rev. B Condens. Matter Mater. Phys.*, 2011, vol. 83, pp. 10–13.
37. R.O. Williams: *Trans. Met. Soc. AIME*, 1958, pp. 212.
38. Y.Z. Vintaykin and A.A. Loshmanov: *Fiz. Metal. Metalloved.*, 1966, vol. 22, pp. 473–76.
39. T.F. Kelly and D.J. Larson: *MRS Bull.*, 2012, vol. 37, pp. 150–58.
40. B. Gault, M.P. Moody, J.M. Cairney, and S.P. Ringer: *Atom Probe Microscopy*, Springer, New York, 2012.
41. R.K. Heenan, J. Penfold, and S.M. King: *J. Appl. Crystallogr.*, 1997, vol. 30, pp. 1140–47.
42. G.D. Wignall and F.S. Bates: *J. Appl. Crystallogr.*, 1987, vol. 20, pp. 28–40.
43. J. Odqvist, J. Zhou, W. Xiong, P. Hedström, M. Thuvander, M. Selleby, and J. Agren: in *1st International Conference on 3D Materials Science*, M.D. Graef, H.F. Poulsen, A. Lewis, J. Simmons, and G. Spanos, eds., The Minerals, Metals & Materials Society, 2012, pp. 221–26.
44. A. Guinier and G. Fournet: *Small-Angle Scattering of X-Rays*, Wiley, New York, 1955.
45. K. Binder and D. Stauffer: *Phys. Rev. Lett.*, 1974, vol. 33, pp. 1006–09.
46. J. Marro, A.B. Bortz, M.H. Kalos, and J.L. Lebowitz: *Phys. Rev. B*, 1975, vol. 12, pp. 2000–11.
47. J. Marro, J.L. Lebowitz, and M.H. Kalos: *Phys. Rev. Lett.*, 1979, vol. 43, p. 282.
48. I.M. Lifshitz and V.V. Slyozov: *J. Phys. Chem. Solids*, 1961, vol. 19, pp. 35–50.
49. C. Wagner: *Z. Elektrochem*, 1961, vol. 65, pp. 581–91.
50. D.A. Huse: *Phys. Rev. B*, 1986, vol. 34, pp. 7845–51.
51. J.G. Amar and F.E. Sullivan: *Phys. Rev. B*, 1988, vol. 37, pp. 196–208.
52. T.T. Rautiainen and A.P. Sutton: *Phys. Rev. B*, 1999, vol. 59, pp. 681–92.
53. S. Abis, R. Caciuffo, F. Carsughi, R. Coppola, M. Magnani, F. Rustichelli, and M. Stefanon: *Phys. Rev. B*, 1990, vol. 42, pp. 2275–81.
54. J.E. Epperson, V.S. Rainey, C.G. Windsor, K.A. Hawick, and H. Chen: *MRS Proc.*, 1990, vol. 205, p. 113.
55. M. Hättestrand, P. Larsson, G. Chai, J.-O. Nilsson, and J. Odqvist: *Mater. Sci. Eng. A*, 2009, vol. 499, pp. 489–92.
56. R.F. Egerton: *Electron Energy-Loss Spectroscopy in the Electron Microscope*, 3rd ed., Springer, New York, 2011.
57. J.W. Cahn: *Acta Metall.*, 1961, vol. 9, pp. 795–801.
58. J.W. Cahn: *Acta Metall.*, 1962, vol. 10, pp. 179–83.
59. J.W. Cahn: *Acta Metall.*, 1963, vol. 11, pp. 1275–82.
60. H. Calderon and G. Kostorz: *MRS Proc.*, 1989, vol. 166, pp. 255–60.
61. M.P. Johansson Jöesaar, N. Norrby, J. Ullbrand, R. M'Saoubi, and M. Odén: *Surf. Coat. Technol.*, 2013, vol. 235, pp. 181–85.
62. E. Eidenberger, M. Schober, P. Staron, D. Caliskanoglu, H. Leitner, and H. Clemens: *Intermetallics*, 2010, vol. 18, pp. 2128–35.
63. J. Langer, M. Bar-on, and H. Miller: *Phys. Rev. A*, 1975, vol. 11, pp. 1417–29.
64. T. Ujihara and K. Osamura: *Phys. Rev. B*, 1998, vol. 58, pp. 371–76.
65. T. Ujihara and K. Osamura: *Mater. Sci. Eng. A*, 2001, vol. 312, pp. 128–35.
66. K. Grönhagen, J. Ågren, and M. Odén: *Scr. Mater.*, 2015, vol. 95, pp. 42–45.